**AFRL-RV-PS-
TR-2015-0126**

**AFRL-RV-PS-
TR-2015-0126**

GROWTH AND CHARACTERIZATION STUDIES OF ADVANCED INFRARED HETEROSTRUCTURES

Sanjay Krishna

**University of New Mexico
1313 Goddard SE
Albuquerque, NM 87106**

30 Jun 2015

Final Report

APPROVED FOR PUBLIC RELEASE; DISTRIBUTION IS UNLIMITED.

**AIR FORCE RESEARCH LABORATORY
Space Vehicles Directorate
3550 Aberdeen Ave SE
AIR FORCE MATERIEL COMMAND
KIRTLAND AIR FORCE BASE, NM 87117-5776**

DTIC COPY

NOTICE AND SIGNATURE PAGE

AFRL-RV-PS-TR-2015-0126 HAS BEEN REVIEWED AND IS APPROVED FOR PUBLICATION IN ACCORDANCE WITH ASSIGNED DISTRIBUTION STATEMENT.

//SIGNED//
CHRISTIAN MORATH
Program Manager

//SIGNED//
PAUL D. LEVAN, Ph.D.
Technical Advisor, Space Based Advanced Sensing and Protection

//SIGNED//
JOHN BEAUCHEMIN
Chief Engineer, Spacecraft Technology Division
Space Vehicles Directorate

REPORT DOCUMENTATION PAGE

Form Approved
OMB No. 0704-0188

1. REPORT DATE *(DD-MM-YY)*	**2. REPORT TYPE**	**3. DATES COVERED** *(From - To)*
30-06-2015	Final Report	15 Feb 2013 – 09 May 2014

4. TITLE AND SUBTITLE
Growth And Characterization Studies Of Advanced Infrared Heterostructures

5a. CONTRACT NUMBER
FA9453-13-1-0284

5b. GRANT NUMBER

5c. PROGRAM ELEMENT NUMBER
63401F

6. AUTHOR(S)

Sanjay Krishna

5d. PROJECT NUMBER
2181

5e. TASK NUMBER
PPM00020523

5f. WORK UNIT NUMBER
EF125696

7. PERFORMING ORGANIZATION NAME(S) AND ADDRESS(ES)

University of New Mexico
1313 Goddard SE
Albuquerque, NM 87106

8. PERFORMING ORGANIZATION REPORT NUMBER

9. SPONSORING / MONITORING AGENCY NAME(S) AND ADDRESS(ES)
Air Force Research Laboratory
Space Vehicles Directorate
3550 Aberdeen Ave., SE
Kirtland AFB, NM 87117-5776

10. SPONSOR/MONITOR'S ACRONYM(S)
AFRL/RVSS

11. SPONSOR/MONITOR'S REPORT NUMBER(S)
AFRL-RV-PS-TR-2015-0126

12. DISTRIBUTION / AVAILABILITY STATEMENT
Approved for public release; distribution is unlimited.

13. SUPPLEMENTARY NOTES

14. ABSTRACT
The goal of this project was to investigate band structure engineering in infared detectors based on Type II superlattice detectors (T2SLs). The origin of high dark current levels in the InAs/In(Ga)Sb T2SL infrared photodetectors was to be investigated. The presence of Shockley-Read-Hall centers degrade the minority carrier lifetime and have been identified as one of the major reasons for the high dark current of T2SL material.

15. SUBJECT TERMS
Carrier lifetime <or> dark current, Shockley-Read-Hall, SRH, superlattice <or> superlattices, type II

16. SECURITY CLASSIFICATION OF:			**17. LIMITATION OF ABSTRACT**	**18. NUMBER OF PAGES**	**19a. NAME OF RESPONSIBLE PERSON**
a. REPORT	**b. ABSTRACT**	**c. THIS PAGE**			Christian Morath
Unclassified	Unclassified	Unclassified	Unlimited	22	**19b. TELEPHONE NUMBER** *(include area code)*

(This page intentionally left blank)

TABLE OF CONTENTS

Section **Page**

LIST OF FIGURES

Figure **Page**

Table **Page**

ACKNOWLEDGMENTS

This material is based on research sponsored by Air Force Research Laboratory under agreement number FA9453-13-1-0284. The U.S. Government is authorized to reproduce and distribute reprints for Governmental purposes notwithstanding any copyright notation thereon.

DISCLAIMER

The views and conclusions contained herein are those of the authors and should not be interpreted as necessarily representing the official policies or endorsements, either expressed or implied, of Air Force Research Laboratory or the U.S. Government.

(This page intentionally left blank)

1 SUMMARY

The goal of this project was to investigate band structure engineering in infared detectors based on Type II superlattice detectors (T2SLs). The origin of high dark current levels in the InAs/In(Ga)Sb T2SL infrared (IR) photodetectors was to be investigated. The presence of Shockley-Read-Hall (SRH) centers degrade the minority carrier lifetime and have been identified as one of the major reasons for the high dark current of T2SL material. The ultimate goal of the program is to decrease the dark current and thereby increase the operating temperature of T2SL detectors through a systematic study involving the growth, fabrication and characterization of T2SL detectors.

This was a very successful project with barrier engineering in interband cascade superlattice detectors and quantum dots in a well detector. The first interband cascade focal plane array (FPA) was reported as a result of this work. There were a total of seven publications that resulted from partial support from this work.

2 INTRODUCTION

We report our experimental investigation on the influence of electron barriers (eBs) in mid-IR interband cascade photodetectors. Even though earlier theoretical projection indicates that an eB with 2-pairs of GaSb/AlSb quantum wells (QWs) is sufficient to block electrons directly tunneling between stages, our experimental results show that a thicker electron barrier (with 6-pairs of GaSb/AlSb QWs) could significantly reduce the device dark current, with little influence on the optical performance. Interband cascade devices with a five stage absorber have demonstrated a dark current density of 8.32×10^{-7} A/cm^2 (at -50 mV), which is within a factor of 2 of the Rule 07 and a Johnson-limited D^* of 1.81×10^{11} cmHz$^{1/2}$/W (at 3.8 μm) at 150K.

Antimony-based T2SLs are being recognized as a viable/competitive alternative to HgCdTe for high-performance IR imaging systems [1]. For the past several years, T2SL technology has received considerable amount of scientific and technological interest. Owing to the great flexibility/versatility of energy band alignment in the nearly lattice-matched "6.1-Å-family" (InAs, GaSb, AlSb, and their alloys) [2], and reduced Auger recombination rate and heavier electron effective masses, various advanced T2SL-based photodetector architectures have been implemented, leading to significantly improved detector performances [3-10]. Among them are the double heterostructures with graded-gap W-structure [3] and M-structure [4], as well as unipolar-barrier detectors [5-6], complementary-barrier IR detectors [7], and interband cascade IR photodetectors (ICIPs) [8-10]. The interband cascade detector has three regions and the principle of operation is shown in Fig. 1. The first is the absorber region in which photo-excited carriers are generated, the second is a hole barrier (hB) that allows transport through electron relaxation and the third is an electron barrier (eB) that enables tunneling into the next stage [10]. The hB typically consists of coupled multi-quantum wells (MQWs), such that a series of stair-case energy ladders is formed in the conduction band. In our design, a type-II broken-gap band alignment between the hB and eB is adopted. Such a design facilitates a fast carrier relaxation path for photo-generated electrons, leading to efficient collection of photo-generated carriers [9-10]. As schematically shown in Fig. 1, due to the existence of the eB on one side (right) of the absorber, combined with the fast relaxation channel at the other side (left), such a preferential electron transport path (left to right in Fig. 1) enables an interband cascade device to have a junction-like rectification behavior and photovoltaic operation [9-11]. The cascade (or multi-junction) scheme has introduced an additional degree of freedom/flexibility for T2SL-based IR detector design, and could potentially open a new dimension for IR photodetector design. While some preliminary experimental results have shown the promising prospect of interband cascade photodetectors, some of the fundamental device physics remains unclear. In such a relatively complicated structure, understanding the underlying device physics as well as finding the optimized design parameters is critical.

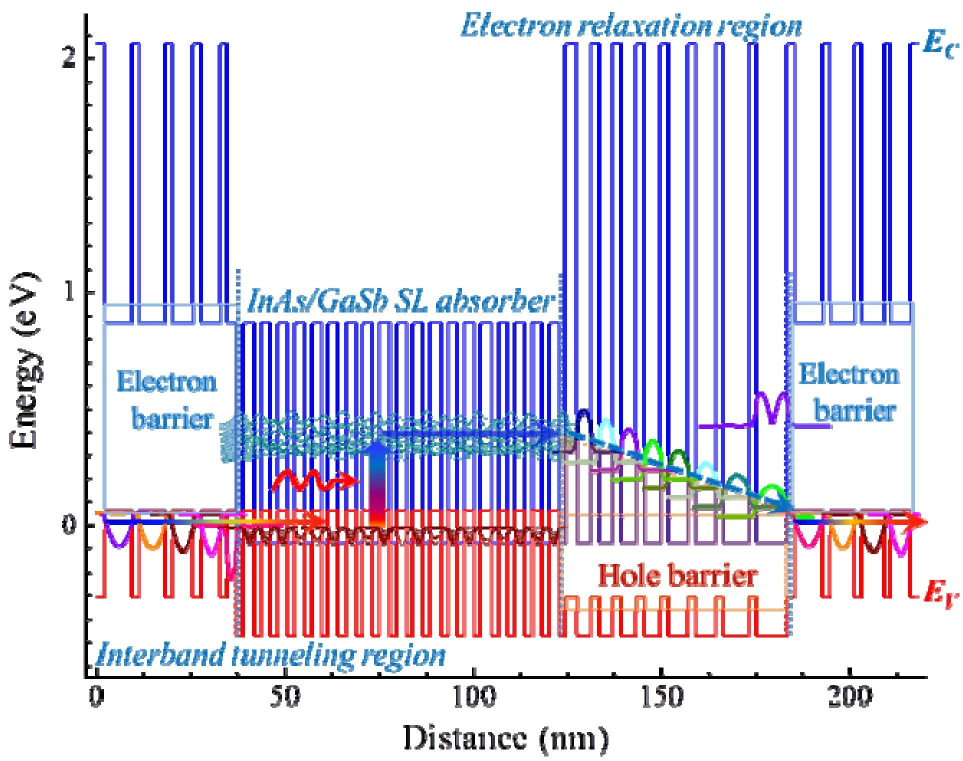

Figure 1. Band diagram of a (simplified) mid-IR interband cascade photodetector relevant envelop wave-functions and their energy levels are also shown.

Figure 1 also shows the structure has been modified for better presentation. The incoming photons are absorbed in the InAs/GaSb SL absorber, generating electron-hole pairs. The electrons will diffuse into the electron relaxation region, and then effectively transport into the valence band of the next stage, through fast longitudinal-optical-phonon-assisted, intraband relaxation and also interband tunneling.

3 *METHODS, ASSUMPTIONS, and PROCEDURES*

In this project, we examined the influence of electron barrier design on the electrical and optical performance of mid-IR interband cascade detectors. As reported in Ref. 10, theoretical investigations based on a two-band $\boldsymbol{k \cdot p}$ model suggest that the estimated direct tunneling time across the double GaSb/AlSb QW is longer than 100 µs. Even though a substantially improved electrical performance was reported and mainly attributed to the "enhanced electron barrier", no qualitative investigations or comparisons were made. It is still unclear whether such a relatively thin electron barrier (~17 nm), as compared to typical unipolar barrier designs (~100-200 nm), is sufficient to block the carriers from passing through. This is especially the case since other transport paths, such as trap-assist tunneling and thermionic emissions, were not included in the modeling. Besides, whether a thicker eB would hinder the photo-carrier transport or would be helpful to properly implement the interband cascade photodetector design needs to be determined. Here, we report our experimental investigation, on the influence of the thickness of the electron barrier on both the electrical and optical performances in mid-IR interband cascade detectors. Devices with different electron barrier thicknesses were designed, grown, fabricated, characterized and analyzed in detail. It was concluded that a thicker electron barrier was instrumental in reducing the dark current, while having no impact on the strength of the optical signal.

The wafers were grown on Zn-doped 2" (001) GaSb substrates with a Veeco Gen-10 solid-source molecular beam epitaxy system, equipped with group III sources and valved group V crackers. The epi-structure starts with a 0.5 µm *p*-type GaSb buffer layer, followed by a 5-stage interband cascade structure with moderately thin InAs/GaSb T2SL as absorber, and terminated with a 45-nm-thick *n*-type InAs top contact layer. Each cascade stage is composed of 30-periods (~140 nm) of non-intentionally doped InAs/GaSb [~6 ML/9 ML (ML = monolayer)] SL absorber, sandwiched between the electron-relaxation and the eB regions. The electron-relaxation region is composed of InAs/Al(In)Sb coupled MQWs to form a stair-case energy ladder in the conduction band, and the separation between adjacent energy levels is designed to be close to the longitudinal-optical-phonon energy [10]. As indicated in Fig. 1, the uppermost energy level in the first InAs QW is close to the conduction miniband in the InAs/GaSb SL, and the bottom energy-level in the final InAs well is positioned below the valence-band edge of the adjacent GaSb layer in the eB region, allowing the interband tunneling of extracted carriers into the next stage. The eB consists of GaSb/AlSb MQWs, and the estimated barrier height in the conduction band is ~0.68 eV. The other role of the GaSb/AlSb MQWs is also the need to facilitate hole transport (in the valence band) towards the type-II broken-gap interface. Three samples with different eB thickness were implemented. Their electron barriers consist of 2-pair, 4-pair, and 6-pair of GaSb/AlSb QWs (the samples will be denoted as 2eB, 4eB, and 6eB hereafter), with each layer thicknesses slightly adjusted for smooth hole transport. The nominal thicknesses of the eB layers are 17, 33 and 48 nm for the 2eB, 4eB and 6eB samples, respectively.

4 RESULTS and DISCUSSION

After growth, the epitaxial wafers were characterized by x-ray diffraction to monitor crystal quality and layer thicknesses. The estimated InAs/GaSb SL periods are about 47.7 Å (2.1% thicker than designed), with full width half maximum of around 30 arc-seconds. The overall strain is controlled within 50 arc-seconds for all the samples. The three samples were then processed into deep-etched mesa-type photodiodes, by using standard contact ultraviolet lithography and wet-chemical etching. The circular mesa-size ranged from 25 to 400 µm in diameter. A 200-nm-thick SiN_x film was then deposited for sidewall passivation and isolation. Top and bottom contacts were formed by e-beam evaporated Ti/Au. No anti-reflectance coating was applied on top of the mesa. Devices were mounted on ceramic leadless chip carriers, and then mounted in the cryostat to characterize their optical and electrical properties.

The electrical performances of the three ICIP devices are characterized over a wide range of temperatures. The dark current densities at -50 mV are as low as 4.24 nA/cm^2 at 80 K and 0.83 µA/cm^2 at 150 K which is comparable to the reported state-of-the-art values [12]. Note that the dark current at lower temperatures could be overestimated due to the setup limitation and imperfect cold shielding. Figure 2 shows the dark current density of the three ICIP devices as a function of voltage at various temperatures. As indicated in the figure, at lower temperatures, devices with thicker eB have significantly lower dark current, particularly under higher operating bias. We believe that such a steeper slope with respect to the operation bias could be an indication that tunneling might be one of the primary dark current components in the thinner devices. As the temperature increases, the difference becomes marginal, which could be an indication that the generation-recombination (G-R) or diffusion current is becoming dominate at higher temperatures.

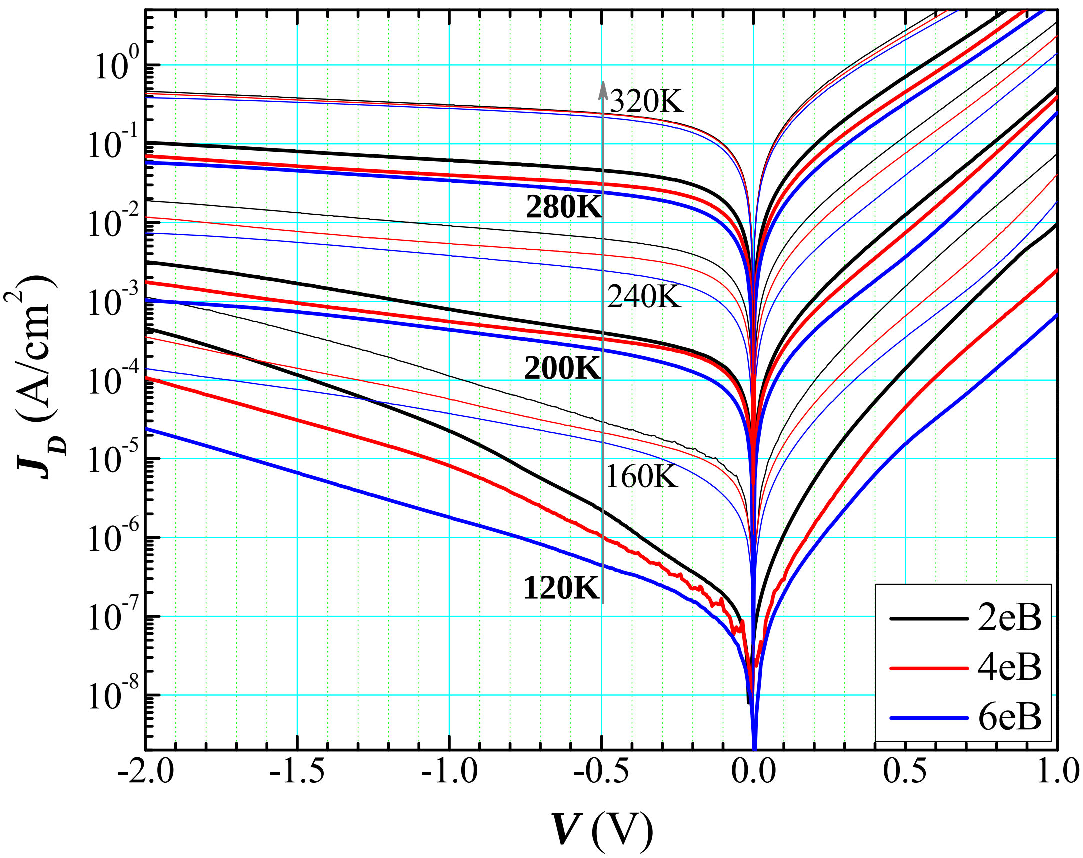

Figure 2. The dark current density of the mid-IR interband cascade detectors as functions of bias voltages at various temperatures. Each of the operation temperatures is labeled near the *J-V* curves.

Figure 3 shows the Arrhenius plot of dark current density at -50 mV as well as the dynamic resistance-area product (R_0A) of three samples. As one can see from Fig. 3, the sample with the thicker eB shows appreciable influence on the dark current density for temperatures up to 280 K, even under lower operating bias. The dark current density is 9.27×10^{-9} A/cm^2 for the 6eB sample at 100 K, and 4.35×10^{-8} A/cm^2 for the 2eB sample. The R_0A of the 6eB sample exceeds 6.15×10^{7} Ωcm^2 at 100 K (42 times higher compared with the 2eB sample), and 2.10×10^{4} Ωcm^2 at 150 K (over 3-times higher than the 2eB sample), which is also comparable to the reported state-of-the-art T2SL detectors [12]. The dark current is as low as 1.98×10^{-6} A/cm^2 at 160 K, which is a factor of two greater than the dark current predicted for HgCdTe by "Rule 07" [13]. At temperatures higher than 280 K, the device performances start to converge as the dark current is less sensitive to the eB thicknesses. As stated earlier, the marginal difference attributed to the dark current is mostly due to G-R or diffusion components.

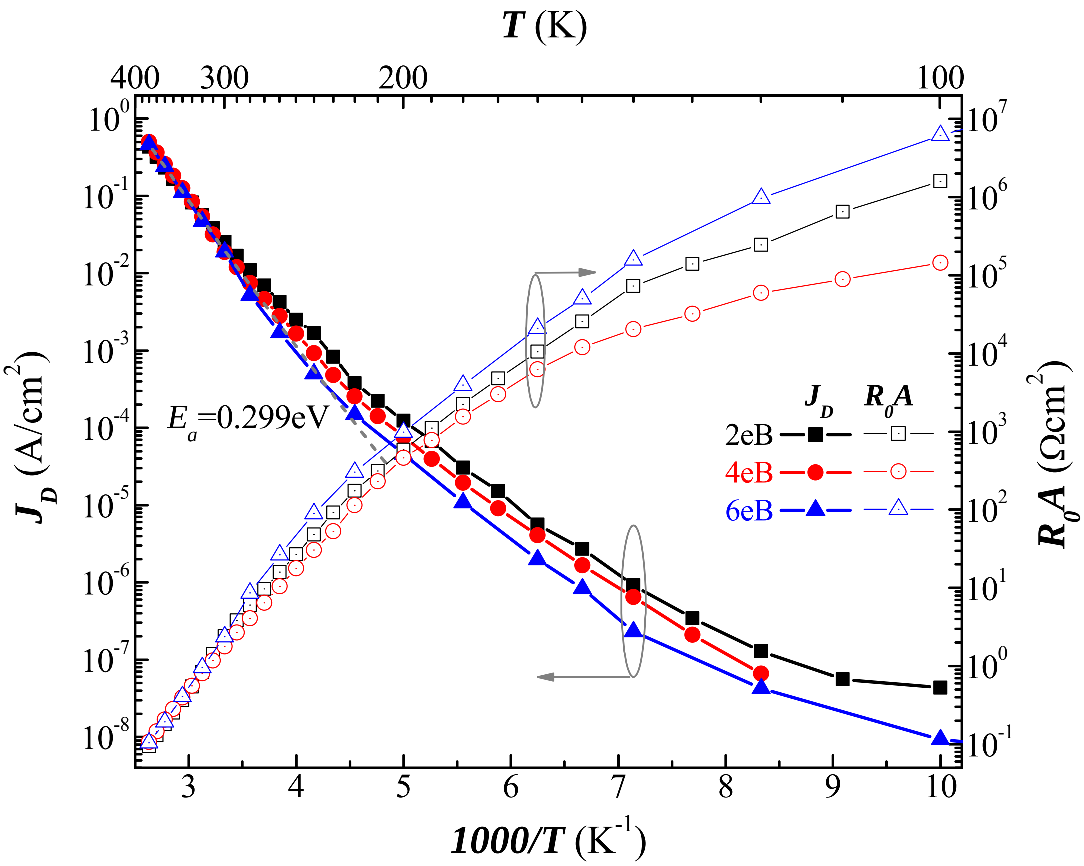

Figure 3. The Arrhenius plots of the electrical performances of the ICIPs, the dark current density (measured at -50 mV) as well as zero-bias resistance-area-product under various temperatures are shown.

The response spectra were obtained from a Fourier-transform IR spectrometer, and were calibrated by radiometric measurements with a black-body at 1000 K. Figure 4a shows the calibrated optical responsivity spectra of samples under zero-bias at various temperatures. The 100% cut-off wavelength of the ICIPs is around 4.2 µm at 80 K, and 4.8 µm at 300 K. The relatively low responsivity is attributed to the relatively thin absorber (the total thickness is 0.7 µm) and the 1/N (N is the number of stages) photoconductive gain inherently due to the interband cascade scheme [9]. As seen in Fig. 4b, the responsivities of the ICIPs at zero-bias are around 0.10 A/W at 3.6 µm and 80 K, then gradually decrease down to 0.08 A/W around 160 K, and then ramp up to 0.13 A/W at temperatures up to 360 K. The thin lines with smaller symbols in Fig. 4b are the responsivities of each of the devices at moderately high reverse bias where the response at 3.6 µm starts to saturate. The saturation responsivity increased from ~0.11 A/W at 80 K, which corresponds to an absorption quantum efficiency of 13.3%, to ~0.13 A/W at 200 K. It is believed that the decrease of zero-bias responsivity at moderate temperatures is due to the background carrier concentration change and p-type to n-type inversion [14]. Such change could introduce some band-bending, which would alter the band alignment and could produce unwanted carrier blocking barriers and deteriorate the zero-bias photo-carrier transport. With the assistance of a stronger reverse bias, more photo-carriers will be collected with the aid of drift, resulting in a monotonic increase in the saturated responsivity.

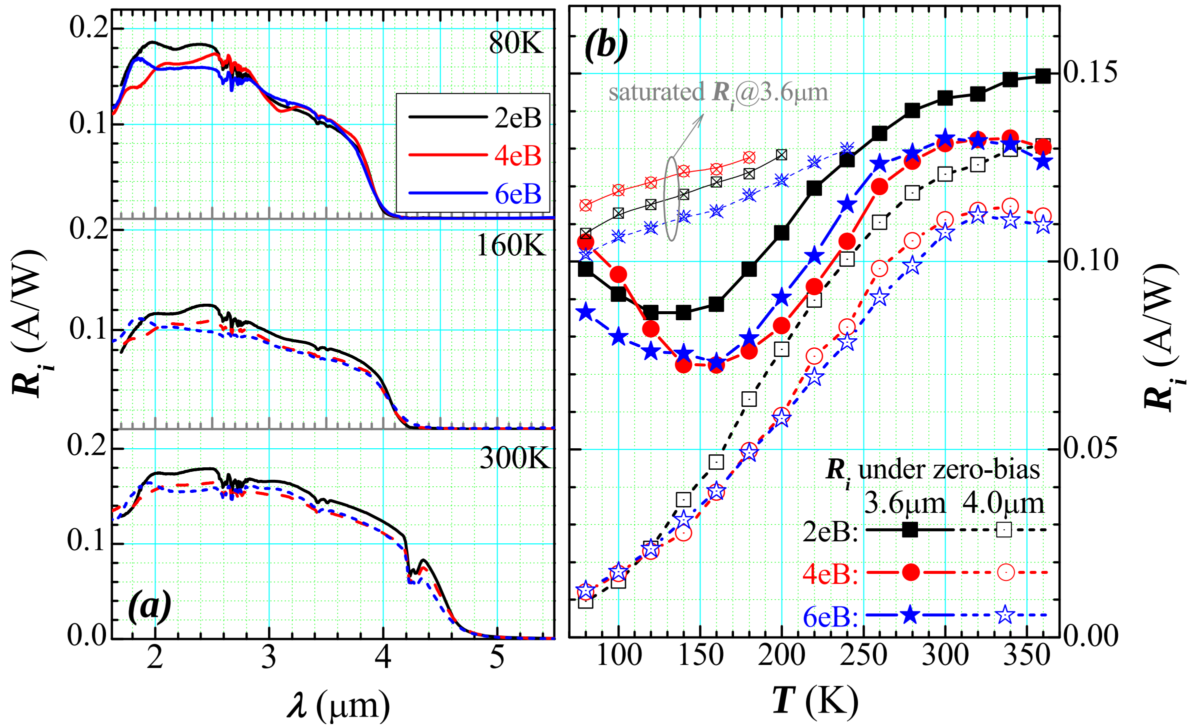

Figure 4. Optical performances of the interband cascade devices under various operation temperatures.

In Figure 4 (a) the response spectra measured at zero-bias at different temperatures and (b) the zero-bias responsivity at 3.6 and 4.0 μm as a function of operation temperature. The saturated R_i at 3.6 μm at lower temperatures are also shown.

In contrast to unipolar barrier detectors, which are typically operated at a slight reversed bias (around -0.1 to -0.3 V) for optimum signal-to-noise ratio (SNR), the efficient carrier extraction under zero-bias enables ICIPs to be operated at zero-bias. As shown in Figure 5, even with the un-optimized design, where the signal under zero-bias is only 55-68% of its saturation value, the maximized SNR is obtained under zero-bias. This could be advantageous for IR detection, especially for high temperature operations.

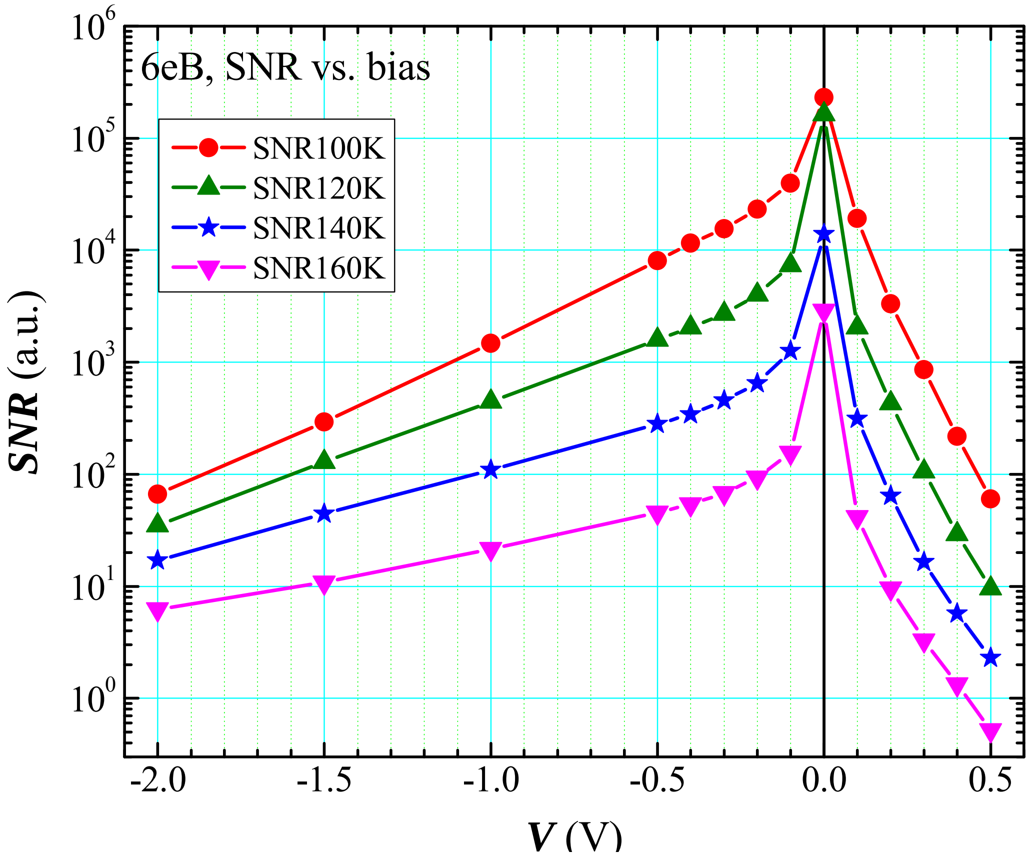

Figure 5. Measured signal-to-noise ratio as a function of bias voltage at various temperatures. The detectors were illuminated using a 1000 K blackbody, the signal modulated by an optical chopper placed in front of the cryostat.

Even with the relatively low responsivity, the improved electrical performances in the ICIP devices lead to improved values of the signal-to-noise ratio and detectivity. Figure 6 is the Johnson-noise limited detectivity spectra for sample 6eB under various temperatures, extracted from the measured responsivity spectra and R_0A. The Johnson-noise limited D^* reaches 8.62×10^{12} Jones at 3.8 μm and 80 K, and 9.73×10^{10} Jones at 160 K. Table 1 summarizes the optical and electrical performance of all samples at different temperatures. The dark current density at -50 mV is 4.57×10^{-5} A/cm^2 at 200 K, and the extracted R_0A is 983 Ω cm^2, corresponding to a Johnson-noise limited D^* of 2.40×10^{10} Jones at 3.8 μm. Preliminary attempts of 320 × 256 FPAs were made on the 4eB and 6eB samples. The FPAs were operational at temperatures up to 150 K, with noise-equivalent temperature differences as low as 20 mK at 80 K. Further investigations are underway and will be reported elsewhere.

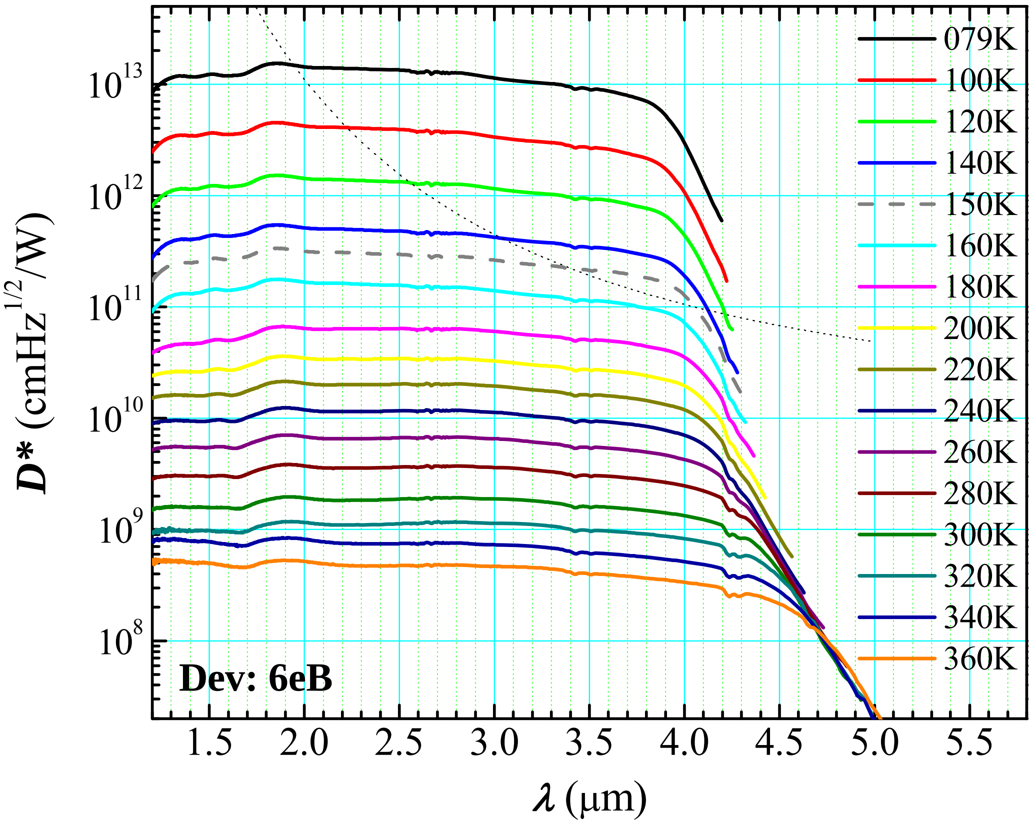

Figure 6. Johnson-noise limited *D spectra of sample 6eB at various temperatures. The background-limited operation temperature is estimated to be around 150 K.**

Table. 1 Electrical and optical performances of the mid-wave ICIPs.

T (K)	Device 2eB				Device 4eB				Device 6eB			
	J_D@-50mV (A/cm^2)	R_0A (Ωcm^2)	R_i@4μm (A/W)	$D^*_{Johnson}$ (Jones)	J_D@-50mV (A/cm^2)	R_0A (Ωcm^2)	R_i@4μm (A/W)	$D^*_{Johnson}$ (Jones)	J_D@-50mV (A/cm^2)	R_0A (Ωcm^2)	R_i@4μm (A/W)	$D^*_{Johnson}$ (Jones)
150	2.71E-6	1.20E4	0.085	1.08E11	1.66E-6	2.56E4	0.070	1.47E11	8.32E-7	4.99E4	0.073	2.22E11
200	1.23E-4	4.61E2	0.107	2.18E10	7.63E-5	5.84E2	0.082	1.88E10	4.57E-5	9.83E2	0.090	2.67E10
300	2.53E-2	1.77	0.143	1.48E9	1.88E-2	2.39	0.132	1.74E9	1.90E-2	2.38	0.132	1.58E9

5 CONCLUSIONS

In summary, the influence of electron barrier design, on the electrical and optical properties of mid-IR interband cascade photodetectors, was evaluated. Our experimental investigations showed that the further enhancement of the electron barrier will significantly reduce the device dark current, with little influence on optical performance. Our results also indicate that a slightly-doped InAs/GaSb T2SL would reduce the influence of background carrier concentration variation with temperature, and would be preferential for consistent temperature behavior. Further investigation is required to find the optimum electron barrier designs. The improvements in the electrical performance have led to substantial performance improvements. An R_0A of 4990 Ωcm^2 and Johnson-limited D^* of 1.82×10^{11} $cmHz^{1/2}/W$ at 3.8 µm at 150 K were obtained. It is believed that the great versatility of the interband cascade photodetectors could be further explored for application-targeted optimization and high performance IR imaging applications.

REFERENCES

1. A. Rogalski, J. Antoszewski, and L. Faraone, "Third-generation infrared photodetector arrays," *J. Appl. Phys.* **105** ,091101 (2009).
2. H. Kroemer, "The 6.1 angstrom family (InAs, GaSb, AlSb) and its heterostructures: a selective review," *Physica E* **20**, 196, (2004).
3. I. Vurgaftman, E.H. Aifer, C.L. Canedy, J.G. Tischler, J.R. Meyer, J.H. Warner, E.M. Jackson, G. Hildebrandt, and G.J. Sullivan, "Graded band gap for dark-current suppression in long-wave infrared W-structured type-II superlattice photodiodes," *Appl. Phys. Lett.* **89**, 121114 (2006).
4. B.-M. Nguyen, M. Razeghi, V. Nathan, and G.J. Brown, "Type-II M structure photodiodes: an alternative material design for mid-wave to long wavelength infrared regimes," *Proc. SPIE* **6479**, 64790S (2007).
5. S. Maimon, and G.W. Wicks, "nBn detector, an infrared detector with reduced dark current and higher operating temperature," *Appl. Phys. Lett.* **89**, 151109 (2006).
6. B.-M. Nguyen, S. Bogdanov, S. Abdollahi Pour, and M. Razeghi, "Minority electron unipolar photodetectors based on type II InAs/GaSb/AlSb superlattices for very long wavelength infrared detection," *Appl. Phys. Lett.* **95**, 183502 (2009).
7. D.Z.-Y. Ting, C.J. Hill, A. Soibel, S.A. Keo, J.M. Mumolo, J. Nguyen, and S.D. Gunapala, "A high-performance long wavelength superlattice complementary barrier infrared detector," *Appl. Phys. Lett.* **95**, 023508 (2009).
8. J.V. Li, R.Q. Yang, C.J. Hill**,** and S.L. Chuang, "Interband cascade detectors with room temperature photovoltaic operation," *Appl. Phys. Lett.* **86**, 101102 (2005).
9. R.Q. Yang, Z. Tian, Z. Cai, J.F. Klem, M.B. Johnson, and H.C. Liu, "Interband-cascade infrared photodetectors with superlattice absorbers," *J. Appl. Phys.* **107**, 054514 (2010).
10. Z. Tian, R.T. Hinkey, R.Q. Yang, Y. Qiu, D. Lubyshev, J.M. Fastenau, Amy W.K. Liu, and M.B. Johnson, "Interband cascade infrared photodetectors with enhanced electron barriers and p-type superlattice absorbers," *J. Appl. Phys.* **111**, 024510 (2012).
11. R.Q. Yang, Z. Tian, J.F. Klem, T.D. Mishima, M.B. Santos, and M.B. Johnson, "Interband cascade photovoltaic devices," *Appl. Phys. Lett.* **96**, 063504 (2010).
12. S. Abdollahi Pour, E.K. Huang, G. Chen, A. Haddadi, B.-M. Nguyen, and M. Razeghi, "High operating temperature midwave infrared photodiodes and focal plane arrays based on type-II InAs/GaSb superlattices," *Appl. Phys. Lett.* **98**, 143501 (2011).
13. W.E. Tennant, "“Rule 07” Revisited: Still a Good Heuristic Predictor of p /n HgCdTe Photodiode Performance?" *J. Electron. Mater.* **39**, 1030 (2010).
14. C. Cervera, J.B. Rodriguez, J.P. Perez, H. Aït-Kaci, R. Chaghi, L. Konczewicz, S. Contreras, and P. Christol, "Unambiguous determination of carrier concentration and mobility for InAs/GaSb superlattice photodiode optimization," *J. Appl. Phys.* **106**, 033709 (2009).

APPENDIX

Publications Resulting From This Effort

1. Tian, Z. B., Schuler-Sandy, T., & Krishna, S. (2013). Electron barrier study of mid-wave infrared interband cascade photodetectors. Applied Physics Letters, 103(8), 083501.

2. Tian, Z. B., Godoy, S. E., Kim, H. S., Schuler-Sandy, T., Montoya, J. A., & Krishna, S. (2014). High operating temperature interband cascade focal plane arrays. Applied Physics Letters, 105(5), 051109.

3. Tian, Z. B., Schuler-Sandy, T., Godoy, S. E., Kim, H. S., & Krishna, S. (2013, September). High-operating-temperature MWIR detectors using type II superlattices. In SPIE Optical Engineering+ Applications (pp. 88670S-88670S). International Society for Optics and Photonics.

4. Tian, Z. B., Schuler-Sandy, T., Godoy, S. E., Kim, H. S., Montoya, J., Myers, S., & Krishna, S. (2013, June). Quantum-engineered mid-infrared type-II InAs/GaSb superlattice photodetectors for high temperature operations. In SPIE Defense, Security, and Sensing (pp. 87041T-87041T). International Society for Optics and Photonics.

5. Acosta, L., Klein, B., Tian, Z. B., Frantz, E., Myers, S., Gautam, N., ... & Krishna, S. (2014, February). Investigation of quantum efficiency in mid-wave infrared (MWIR) InAs/GaSb type-II strained layer superlattice (T2SL) detectors. In SPIE OPTO (pp. 89960P-89960P). International Society for Optics and Photonics.

6. Kim, J. O., Ku, Z., Kazemi, A., Urbas, A., Kang, S. W., Noh, S. K., ... & Krishna, S. (2014). Effect of barrier on the performance of sub-monolayer quantum dot infrared photodetectors. Optical Materials Express, 4(2), 198-204.

7. Kim, J. O., Ku, Z., Krishna, S., Kang, S. W., Lee, S. J., Jun, Y. C., & Urbas, A. (2014). Simulation and analysis of grating-integrated quantum dot infrared detectors for spectral response control and performance enhancement. Journal of Applied Physics, 115(16), 163101.

LIST OF ACRONYMS

eB	electron barrier
FPA	Focal plane array
G-R	generation-recombination
hB	hole barrier
ICIP	interband cascade infrared photodetectors
IR	Infrared
ML	monolayer
MQW	multi-quantum well
QW	quantum well
SRH	Shockley-Read-Hall
SNR	signal-to-noise ratio
T2SL	type-II superlattice

DISTRIBUTION LIST

DTIC/OCP 8725 John J. Kingman Rd, Suite 0944 Ft Belvoir, VA 22060-6218	1 cy
AFRL/RVIL Kirtland AFB, NM 87117-5776	2 cys
Official Record Copy AFRL/RVSS/Christian Morath	1 cy